NEOPLASIA
www.neoplasia.com

Volume 22 Number 12 December 2020 pp. 770–777

Noninvasive multiparametric characterization of mammary tumors with transmission-reflection optoacoustic ultrasound ☆,1,2

Berkan Lafci [a]; Elena Merčep [b,c]; Joaquin L. Herraiz [d,e]; Xosé Luís Deán-Ben [a]; Daniel Razansky [a,b,*]

[a] Institute for Biomedical Engineering and Institute of Pharmacology and Toxicology, University of Zurich and ETH Zurich, Zurich, Switzerland
[b] Institute for Biological and Medical Imaging, Technical University of Munich and Helmholtz Center Munich, Neuherberg, Germany
[c] iThera Medical GmbH, Munich, Germany
[d] Nuclear Physics Group and IPARCOS, Complutense University of Madrid, Madrid, Spain
[e] Health Research Institute of Hospital Clínico San Carlos (IdISSC), Madrid, Spain

Abstract

Development of imaging methods capable of furnishing tumor-specific morphological, functional, and molecular information is paramount for early diagnosis, staging, and treatment of breast cancer. Ultrasound (US) and optoacoustic (OA) imaging methods exhibit excellent traits for tumor imaging in terms of fast imaging speed, ease of use, excellent contrast, and lack of ionizing radiation. Here, we demonstrate simultaneous tomographic whole body imaging of optical absorption, US reflectivity, and speed of sound (SoS) in living mice. In vivo studies of 4T1 breast cancer xenografts models revealed synergistic and complementary value of the hybrid imaging approach for characterizing mammary tumors. While neovasculature surrounding the tumor areas were observed based on the vascular anatomy contrast provided by the OA data, the tumor boundaries could be discerned by segmenting hypoechoic structures in pulse-echo US images. Tumor delineation was further facilitated by enhancing the contrast and spatial resolution of the SoS maps with a full-wave inversion method. The malignant lesions could thus be distinguished from other hypoechoic regions based on the average SoS values. The reported findings corroborate the strong potential of the hybrid imaging approach for advancing cancer research in small animal models and fostering development of new clinical diagnostic approaches.

Neoplasia (2020) 22, 770–777

Keywords: Ultrasound computed tomography, Optoacoustic imaging, Photoacoustics, Preclinical imaging of tumors, Speed of sound imaging, Cancer research

Introduction

Breast cancer is the most frequent noncutaneous type of cancer in women and the second cause of cancer-related deaths in the female population [1]. Imaging-based mammography screening is considered to be a major factor leading to a 15% to 30% reduction of breast cancer mortality [2]. X-ray imaging of the breast remains the gold standard for breast screening in the clinical setting. Yet, this approach involves exposure to ionizing radiation and pain caused by breast compression. Moreover, false positives are produced, e.g., due to the presence of cysts [3] and the sensitivity is low in women with radiographically dense breast [4]. Magnetic resonance imaging and pulse-echo (reflection) ultrasound (US) are then also routinely used in the clinics to complement the drawbacks of x-ray mammography. Magnetic resonance imaging provides high sensitivity for the detection of breast cancer, yet it attains low specificity and comes with high operational costs [5]. Pulse-echo US can distinguish between liquid-filled cysts from solid masses and even detect tumors not visible in x-ray images [6]. However, standard hand-held scans are operator dependent, which prevents the wide use of US as a standalone method.

* Corresponding author.
E-mail address: daniel.razansky@uzh.ch (D. Razansky).

☆ *Abbreviations*: AA, acoustic attenuation, DAQ, data acquisition system, FOV, field of view, FWI, full-wave inversion, MSOT, multispectral optoacoustic tomography, OA, optoacoustic, RUCT, reflection ultrasound computed tomography, SoS, speed of sound, TOF, time-of-flight, TROPUS, transmission-reflection optoacoustic ultrasound, US, ultrasound.

[1] Declaration of Competing Interest: The authors declare that they have no known competing financial interests or personal relationships that could have appeared to influence the work reported in this paper.

[2] Funding: This work was supported by grants from the German Research Foundation (RA1848/5-1) and the Swiss Data Science Center (C19-04). J. L. Herraiz acknowledges support from the Spanish Ministry of Science and Innovation, grant RTI2018-095800-A-I00.
Received 20 August 2020; received in revised form 9 October 2020; accepted 12 October 2020

https://doi.org/10.1016/j.neo.2020.10.008

In recent years, multispectral optoacoustic tomography (MSOT) imaging has been shown to significantly enhance the capabilities of pulse-echo US for the detection of breast carcinomas [7]. Identification of tumors in MSOT images is facilitated by key biomarkers such as local increases in vessel density around the tumor region [8,9], changes in oxygen saturation in the tumor microenvironment [10,11] or alterations in the local distribution of fat, collagen, and other intrinsic tissue chromophores [12]. The MSOT imaging depth is maximized for optical wavelengths around 1064 nm due to relatively low scattering and absorption of light by living tissues and the high energy of commonly available lasers at this wavelength [13]. However, optoacoustic (OA) imaging is generally incapable of accurate delineation of tumor shape and boundaries. Complementary anatomical information can be provided with pulse-echo US images rendered with hybrid systems [14,15,16]. Also, US imaging can be performed in transmission mode, in which case additional important mechanical and elastic tissue parameters can be extracted, such as maps of speed of sound (SoS) and acoustic attenuation (AA) [17]. Recent studies showed that SoS maps provide a powerful means to identify the tumor volume [18,19], while AA maps can provide enhanced contrast for different tissue types [20].

In this work we employ a trimodal transmission-reflection optoacoustic ultrasound (TROPUS) imaging platform for simultaneous characterization of solid tumors in mice. The imaging approach is based on a full ring of cylindrically focused transducers that can provide high-resolution cross-sectional OA images in real time by exciting the tissue with a single laser pulse. Sequential excitation of the array elements and detection of the reflected and transmitted US waveforms further enables forming pulse-echo US as well as SoS images. We further employed a full-wave inversion (FWI) method for reconstructing the transmission US data [17], which resulted in enhanced contrast and resolution as compared to the previously reported TROPUS implementation [21].

Materials and methods

The imaging setup

The experimental set-up employed for image acquisition consists of 4 main modules, namely, a high-speed active transmission and data acquisition system (DAQ), an US ring-shaped transducer array, a pulsed laser source and a workstation computer (Figure 1a). OA pressure waves are generated by illuminating the tissues with a nanosecond Nd:YAG pumped laser source (Spectra-Physics, Santa Clara, CA, USA) operating at 15 Hz pulse repetition rate. The full-ring-shaped transducer array was custom engineered (Imasonic Sas, Voray, France) for tomographic cross-sectional small animal imaging. It consists of 512 cylindrically focused transducer elements with dimensions 0.37×15 mm^2 and interelement pitch of 0.47 mm. All the transducer elements are distributed equidistantly on 2 arcs, each covering a 174° angle. The radius of curvature is 40 mm and every single transducer element is cylindrically focused at 38 mm distance (x–z plane in Figure 1a) to create a cross-sectional imaging geometry. The peak central frequency and transmission/reception bandwidth of the array elements at −3 dB are 5 MHz and 60%, respectively. The US array generates pressure waves used to interrogate the imaged sample in transmission US imaging mode while also detecting the pressure waves transmitted/reflected or generated within the imaged cross section in the pulse-echo US and OA modes, respectively. In the US transmission mode, the excitation pulses are transmitted by the DAQ to each element of the array to generate US waves. When DAQ is switched to the receive mode, the detected pressure signals collected by the elements of the transducer array are digitized and transmitted over 1 Gbit/s Ethernet connection to the host PC. Digitization sampling rate of 40 megasamples per second and vertical resolution of 12 bits were used for data acquisition. For collecting 3D image data, the US array was translated in the vertical direction (y axis in Figure 1a) with 1 mm step size using a motorized stage. For mouse imaging, the array was placed inside a temperature-controlled (34 °C) water tank to increase the acoustic coupling efficiency between the imaged object and US sensors. The workstation computer having 128 GB of random access memory and NVIDIA GeForce GTX 1060 graphical processing unit synchronizes the DAQ and the laser by setting the transmission parameters and controlling reception events. It is also used to record and process the acquired signals to reconstruct images.

Optoacoustic tomography

OA tomographic imaging of mice was performed at 1064 nm as this particular wavelength is known to have deep penetration into living mammalian tissues [13]. A fiber bundle (LightGuideOptics GmbH, Rheinbach, Germany) separated into 12 output ferules on its distal end was used to deliver the light beam from the laser output to the imaging sample. For this, 6 output ferules were placed with 60° separation (equidistantly) on each side of the transducer array (Figure 1a) to facilitate uniform light delivery to the imaged mouse cross section. The output ferules of the bundle having 0.21×12.65 mm^2 dimensions were tilted 24° to attain an illumination ring with an area of 6 cm^2 upon the mouse surface. The pressure waves excited within the sample were received with 512 elements after every laser pulse and simultaneously digitized with the DAQ. OA images over a field of view (FOV) of 25×25 mm^2 were reconstructed using a back-projection algorithm after band-pass filtering the raw data in the 0.5 to 6 MHz frequency range [22]. The mouse boundary was manually segmented in the OA images to suppress the background. The images were subsequently normalized with a modified Bessel-function that was previously shown to approximate well the diffuse light distribution within a homogenous scattering and absorbing cylinder [23]. Finally, a vesselness (Frangi) filter was applied on the images to increase the vascular contrast [24].

Reflection (pulse-echo) ultrasound computed tomography

US imaging was performed by sending a short pulse consisting of one cycle of bipolar signal (20 V_{pp}) with duration of 0.16 μs to each element of the array in every transmission event. The transmission events were repeated to transmit pressure signals with all array elements. In one transmission event, the DAQ can transmit with a single element and receive reflected or transmitted signals from other 128 elements. Thereby, the pulse transmission events for each element were repeated 4 times so that the signals from all 512 elements (360° full coverage) are acquired. The reflection US computed tomography (RUCT) images were reconstructed with the synthetic transmit aperture technique. Synthetic transmit aperture uses different single element in each transmission event and then coherently compounds the images from those transmission events to form the final image [25,26]. For the beam-forming process, 64 elements located to the left and 64 elements to the right from the transmitting element were included. In total 129 channels including the signals detected by the transmitting element were used for reconstruction of one subframe for every transmission event. The standard delay-and-sum algorithm was used for reconstructing low-resolution subframes over 25×25 mm^2 FOV equivalent to that of the OA images. This process resulted in 512 low-resolution images that were acquired by each transmission event, which were then coherently compounded to form the final high-resolution image.

Speed of sound imaging

SoS tomography images were reconstructed from the US waves traversing the sample (mouse). For each transmitting element, the signals collected from 171 elements located on its the opposite side were considered (Figure 1a). SoS maps were reconstructed with a FWI method [17]. A time-of-flight (TOF) picker algorithm was used to calculate the difference between the TOF of waves propagating in water and through the sample [27,28]. This TOF

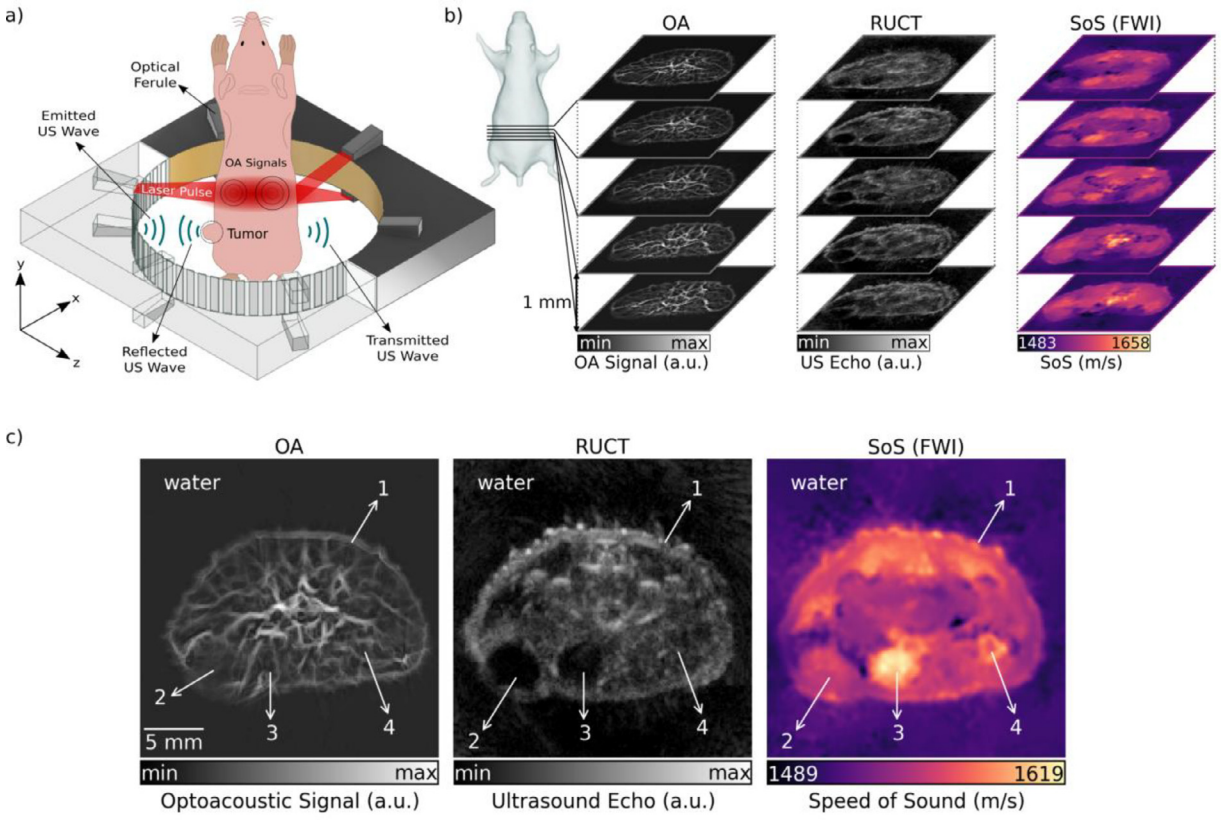

Figure 1. The trimodal transmission reflection optoacoustic ultrasound (TROPUS) imaging platform. (a) Excitation and acquisition steps in the optoacoustic (OA) imaging mode, reflection ultrasound computed tomography (RUCT) mode, and transmission ultrasound computed tomography (TUCT) speed of sound (SoS) imaging mode. (b) Illustration of 3D stacks of cross-sectional multimodal images acquired noninvasively from tumor-bearing mice. (c) Representative TROPUS images of a cross section of the tumor region in a mouse. From left to right, optoacoustic (OA) image, reflection ultrasound computed tomography (RUCT) image, and speed of sound (SoS) image acquired in the transmission ultrasound computed tomography (TUCT) mode and reconstructed with the full-wave inversion (FWI) method. 1 – Skin, 2 – Tumor, 3 – Urinary bladder, 4 - Femur.

picker algorithm was improved by weighting, median filtering and reciprocal pair comparison of the calculated TOF values, as previously described [29]. The wave propagation model was based on sampling the space between emitter and receiver along multiple paths using a family of Bézier curves. In short, the FWI method convolves a reference waveform with estimated TOF values from different paths corresponding to the defined curves [30]. Then, it minimizes the cost function between simulated waves and the measurements by changing SoS values in the defined image grid. This process is repeated iteratively until the cost function converges. The estimated SoS values provide the corresponding wave propagation speed for the defined cross-sectional reconstruction grid containing the mouse and background medium. Herein, the FWI method was employed to achieve improved resolution and contrast in the transmission US imaging mode as compared to the previously reported TROPUS implementation [21], which used the less accurate bent-rays approach. In the latter case, the wave propagation was significantly simplified and modeled as a narrow ray going through the path with the lowest TOF between the emitter and the receiver. Despite its merits, FWI has high computational complexity, which results in 5 min of reconstruction time per slice when using graphical processing unit. In this study, we further performed a comparison of the SoS maps reconstructed with all the 3 approaches. Transmission US further enables reconstructing AA maps. However, these were not considered in the current study due to lack of valuable tumor-related contrast.

Animal handling

In total, 5 mice of the same age were imaged with the TROPUS system. All mice were anesthetized with 1.8% isoflurane in 100% oxygen flowing at a rate of 0.8 L/min. A custom-designed animal holder was used to keep the imaged mouse in vertical position inside the ring-shaped detector array. The head of the mouse was kept above the water level and a mask was used to deliver the oxygen-anesthesia mixture. The water temperature was maintained at 34 °C during the measurements. One of the mice (M1) was used as a control with no tumor. The other 4 mice had orthotopic tumors induced via inoculation of 4T1 mammary carcinoma cells in the mammary fat pad. Cell inoculation was performed at different days to characterize the ability of the TROPUS system to image tumors at different stages. Specifically, 2 orthotopic tumors in mice M3 and M4 were induced 1 mo before the experiment, while the tumor cells were inoculated 3 wk before the experiment in mice M2 and M5. All procedures involving animal care and experimentation were conducted in full compliance with the institutional guidelines of the Institute for Biological and Medical Imaging and with approval from the Government of Upper Bavaria.

Results

The representative 3D image stacks acquired noninvasively from a tumor-bearing mouse are shown in Figure 1b, corroborating the system's ability to

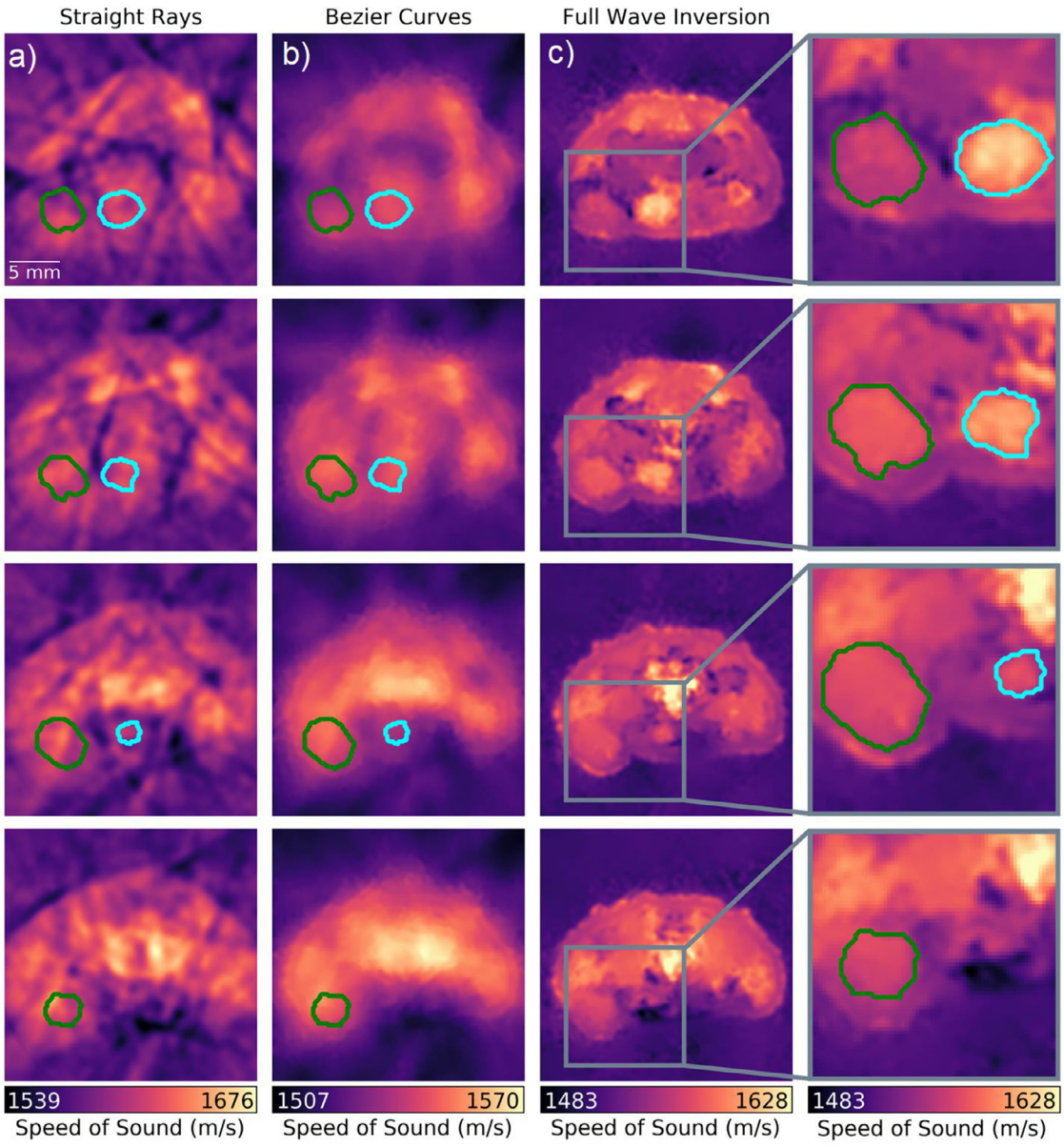

Figure 2. Comparison between different methods for rendering the speed-of-sound (SoS) images with transmission ultrasound computed tomography. (a) Straight ray approximation. (b) Bézier curve reconstruction. (c) Full-wave inversion (FWI). Reconstructions from different cross sections acquired from the same mouse with 1 mm steps are shown – see Figure 1b. The SoS values were calculated over the tumor (green curve) and urinary bladder (cyan curve) areas manually segmented in the FWI images. (For interpretation of the references to color in this figure legend, the reader is referred to the web version of this article.)

simultaneously deliver whole body multimodal OA and US data from mice. Representative cross sections of the OA, RUCT, and SoS images covering 25×25 mm^2 FOV containing the tumor are further shown in Figure 1c. The tumor location can be readily identified as a hypoechoic region in the RUCT image and as a region with lower vessel density in the OA image. In addition, SoS images enable the tissue assessment based on the distribution of its elastic modulus and density.

Note that the quality of the SoS images strongly depends on the inversion method. Indeed, the tumor mass is barely visible in the images reconstructed using straight ray approximation, which generally exhibit size-distortion due to refraction and poor contrast and resolution (first column in Figure 2). When a more accurate modeling approach is attempted for the SoS reconstruction assuming Bézier-curve type of wave propagation, the reconstructed image quality readily improves (second column in Figure 2). In our previous work the Bézier curve approximation was shown to be sufficiently accurate to enable the segmentation of outer boundaries and major anatomical structures [21]. However, quantitative analysis of smaller regions such as tumors cannot reliably be performed with this approach due to insufficient spatial resolution and contrast. While increased values of SoS are observed in the tumor region, similar values also appear in other regions, thus hampering unequivocal tumor differentiation. The state-of-the-art FWI reconstruction method significantly improves the resolution, contrast, and overall quality of the SoS maps (third column in Figure 2), facilitating clear delineation of the tumor boundaries and other anatomical structures. This is also shown in Figure 1c by comparing RUCT and SoS images. Further analysis was done to compare SoS values in different anatomical regions,

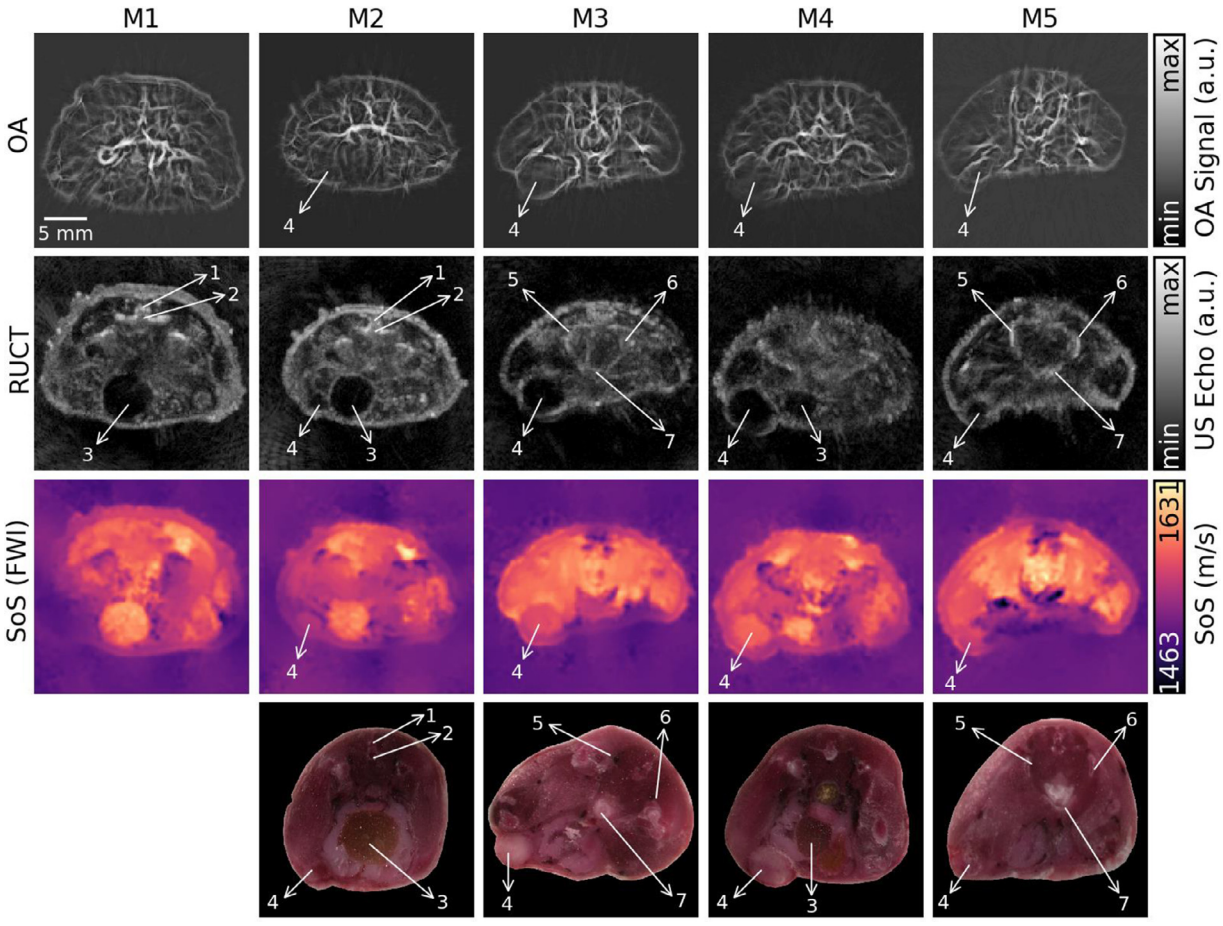

Figure 3. Cross-sectional multimodal images of the tumor-bearing (M2–M5) and tumor-free (M1) mice acquired from approximately the same abdominal region. Histological cryosections taken from approximately corresponding regions ex vivo are shown in the bottom row. The tumors and other anatomical structures are labeled: 1 – Vertebral column, 2 – Caudal vertabrae, 3 – Urinary bladder, 4 – Tumor, 5 – Coxal bone, 6 – Ischium, 7 – Female urethra.

namely tumor and urinary bladder, estimated with each reconstruction method. These anatomical structures were manually segmented in the cross sections rendered with the FWI method. The calculated mean and standard deviation of the SoS values in the tumor were 1614 ± 11.45 m/s, 1544 ± 3.60 m/s, and 1564 ± 6.17 m/s for the straight ray approximation, the Bézier curves method and the FWI method, respectively. The corresponding values for the urinary bladder were 1611 ± 7.84 m/s, 1541 ± 2.14 m/s, and 1584 ± 11.02 m/s. Thus, no clear distinction between the tumor and urinary bladder can be made by analyzing the SoS values rendered with the straight ray and Bézier curves methods, yet such differentiation is possible based on values extracted with the FWI methods. The volumes of the tumor and urinary bladder regions were further estimated by integrating the segmented regions over consecutive slices. This resulted in 219 mm^3 and 196 mm^3 estimates for the tumor and urinary bladder, respectively.

We subsequently analyzed in vivo data from $n = 4$ tumor-bearing mice (M2–M5) and a tumor-free mouse (M1). The results are shown in Figure 3. While vascular density/size is clearly altered in the tumor regions according to the OA data, the lesion boundaries cannot be accurately discerned from those images. The RUCT data are used instead for anatomical guidance and segmentation of the tumor boundaries. Yet, anechoic or hypoechoic structures corresponding to malignant tumors may easily be confused with other mouse organs. For example, the urinary bladder, clearly distinguished as a low intensity region in the RUCT image of M1 (Figure 3), exhibits similar characteristics to tumors regions shown for other mice. In this regard, the additional information provided by OA facilitates classifying this region as benign since no increase in vessel density or thickness occurs around expected tumor region. OA images from M3 and M4 show increased vessel density around the tumor region but not in the tumor core, which is consistent with previous studies [10,31]. However, OA images are often corrupted with streak type artifacts [32] that can be observed in the urinary bladder area. Note that such artifacts are commonly amplified by the Frangi filtering (see image comparison in the supplementary information), which may lead to misinterpreting the artifacts for blood vessels. In general, the streak artifacts can be mitigated by using an imaging system with higher number of elements or employing more sophisticated reconstruction approaches [33]. Note also that the RUCT images of M3 and M4 exhibit several regions with low intensity, which seem to be difficult to classify as benign or malignant even in conjunction with the vascularization information provided by the OA data. This turns even more challenging for M2 and M5, which have small-sized tumors. In those cases, the SoS data may serve as a complementary modality for increasing specificity of tumor detection and characterization. The tumor locations identified by the multimodal in vivo TROPUS imaging were further confirmed by studying the histological cryosections taken from approximately corresponding regions ex vivo (last row in Figure 3). Note that while the anatomical structures visible in the cryosections were generally matching the information obtained by TROPUS, the exact shape and size of the different structures might have changed due to compression and freezing of the samples.

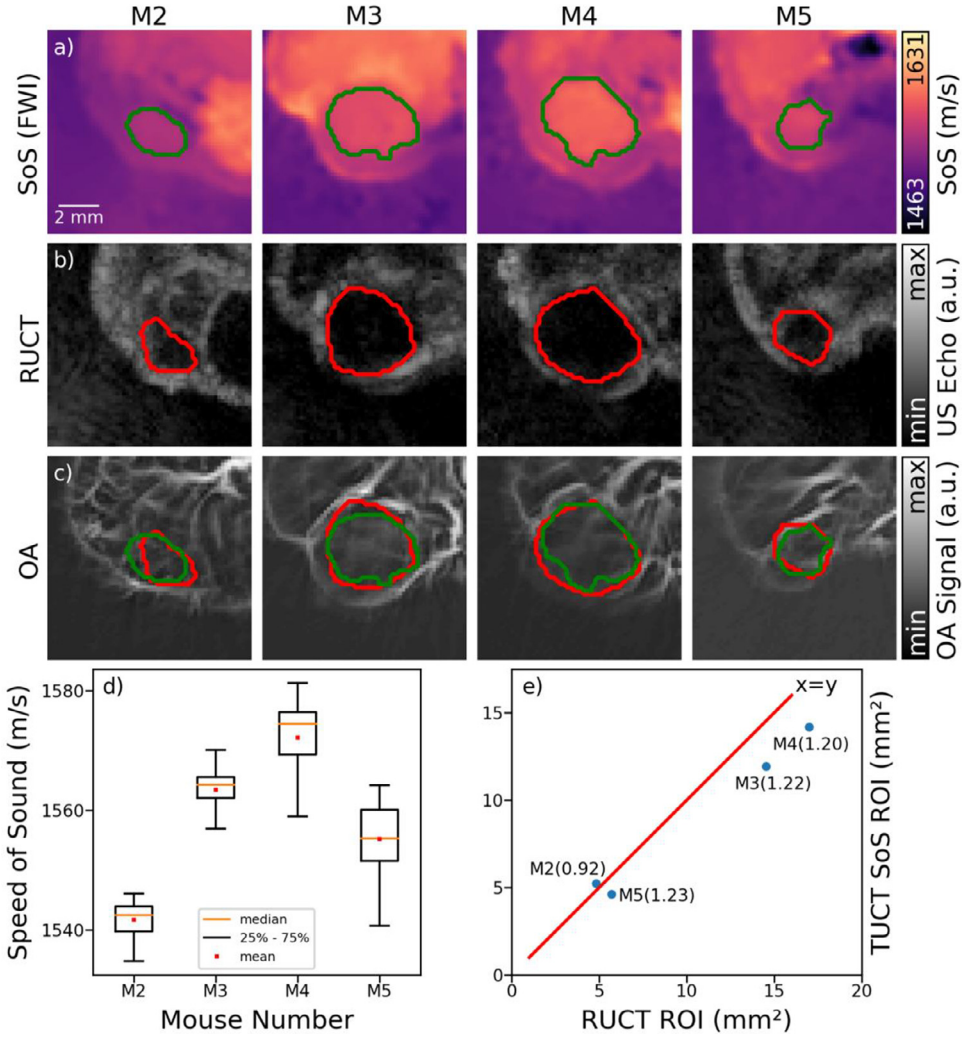

Figure 4. Tumor segmentation and characterization. (a) The manually segmented tumor areas in the SoS images reconstructed with full-wave inversion (FWI) method. (b) The corresponding segmentations based on the reflection ultrasound computed tomography (RUCT) images. (c) The segmented areas superimposed onto the optoacoustic (OA) images. (d) Measured mean and standard deviation of speed of sound (SoS) values inside the segmented ROIs based on SoS-based tumor segmentations. (e) Comparison of the measured tumor areas based on the SoS- and RUCT-based tumor segmentations. The ratios between the calculated areas are presented for each imaged mouse.

To compare the information provided by reflection and transmission US, the tumors were manually segmented in the RUCT and SoS images following their identification and localization using the multimodal data. The segmented regions based on the SoS (Figure 4a) and RUCT (Figure 4b) data were then superimposed on the OA images (Figure 4c). Even though the US-based segmentations generally match the regions with low vessel density in the OA images, robust tumor differentiation based on vascular OA features seems challenging. We subsequently generated binary masks from the segmented region of interests (ROI) and extracted the mean and standard deviation of the SoS values in the tumor regions (Figure 4d). The measured mean SoS values in the tumors ranged from 1541 to 1572 m/s with the respective standard deviations ranging from 2.77 to 6.26 m/s. Also, the SoS values increased as a function of tumor size, though the limited sample size prevents establishing such a correlation unambiguously. In general, the reconstructed SoS values in the tumor regions are in the range of previously reported data for solid breast tumors [34], yet longitudinal study with an increased sample size is needed to validate quantification by the proposed methods.

Finally, the anatomical localization capabilities of the RUCT and SoS images were compared based on the segmented tumor areas from both modalities. While comparison between the extracted tumor areas yields similar values for both modalities (Figure 4e), slightly larger area estimations were generally obtained when segmenting tumors based on the RUCT images in 3 out of 4 tumor-bearing mice. In one mouse having the smallest tumor size (M2), the segmented area was slightly larger in the SoS image, though the actual SoS values were smaller, which may just indicate an early stage of the tumor development.

Discussion and conclusions

The presented results indicate that the marriage between diverse OA and US contrasts in one single TROPUS platform has the potential to provide complementary information for characterizing mammary tumors in mice. Angiogenesis is a central hallmark of solid tumors, representing formation of new vascular networks necessary to support tumor growth and metastasis. In our study, neovasculature was clearly observed in the areas surrounding the tumors in the OA images. However, tumor boundaries could not clearly be discerned based on the vascular anatomy contrast provided by the OA data. On the other hand, the tumors appeared as anechoic or hypoechoic structures

in pulse-echo US, although some mouse organs like the urinary bladder may have a similar appearance in those images. The improved resolution and contrast of SoS maps reconstructed with the FWI method facilitated the delineation of the tumor mass. In this case, we were able to assign the tumors to areas having sharp boundaries and a relatively uniform SoS different from the background. The extracted average values of SoS in the tumor regions could also potentially be used to distinguish malignant lesions from other regions with uniform SoS. Generally, reliable identification of tumors appears to be challenging in images from standalone modalities and the complementary information provided by OA, pulse-echo US and SoS images aided an unambiguous identification. Yet, further work is required to strengthen the synergistic and complementary value of the suggested hybrid imaging methodology.

Even though the present study solely focused on the anatomical imaging capabilities of OA and US, these modalities are generally equipped with a range of additional functional and molecular imaging features that can aid tumor identification and characterization. Previous studies using MSOT approaches have demonstrated high-resolution readings of tumor oxygenation gradients across tumors [35] as well as perfusion and targeted uptake of nanoparticles and other molecular agents by the tumor microenvironment [31,36]. Similarly, Doppler and contrast-enhanced US imaging have been used for multiparametric characterization of functional tumor parameters [37,38,39]. From the imaging point of view, hybridization of multiple modalities based on US and OA excitation can enhance the reconstruction accuracy of those methods by exploiting synergistic information on the underlying optical and acoustic tissue properties [32,40]. The accuracy and quantification capabilities of the proposed system shall be validated in future longitudinal studies.

Clinical translation potential is another important aspect of the TROPUS platform that can be explored for identifying new diagnostics biomarkers of breast cancer. To this end, pulse-echo US is routinely used in the clinics for anatomical guidance and characterization of breast lesions. Transmission US has also shown promising diagnostic results in clinical trials [41]. Initial clinical studies aimed at early breast cancer detection have also been performed with OA imaging [8]. In one recent study, a full-ring array analogous to the one used in the TROPUS system has been tested for OA imaging of human breast [42], further supporting the clinical translation potential of our approach.

In conclusion, we demonstrated the potential of TROPUS imaging for detection and characterization of mammary tumors in mice. The reported findings corroborate the strong potential of the hybrid imaging approach for advancing cancer research in small animal models and fostering development of new clinical diagnostic approaches.

Authors' contributions

Conception and design: E. Merčep, D. Razansky; Development of methodology: B. Lafci, E. Merčep, D. Razansky; Acquisition of data (provided animals, acquired and managed patients, provided facilities, etc.): E. Merčep, D. Razansky; Analysis and interpretation of data (e.g., statistical analysis, biostatistics, computational analysis): B. Lafci, J. L. Herraiz, X. L. Deán-Ben; Writing, review, and/or revision of the manuscript: B. Lafci, J. L. Herraiz, X. L. Deán-Ben, D. Razansky; Study supervision: D. Razansky.

Supplementary materials

Supplementary material associated with this article can be found, in the online version, at doi:10.1016/j.neo.2020.10.008.

References

[1] Siegel RL, Miller KD, Jemal A. Cancer statistics, 2019. *CA Cancer J Clin* 2019;**69**:7–34.

[2] Lam DL, Pandharipande PV, Lee JM, Lehman CD, Lee CI. Imaging-based screening: understanding the controversies. *Am J Roentgenol* 2014;**203**:952–6.

[3] Berg WA, Blume JD, Cormack JB, Mendelson EB, Lehrer D, Böhm-Vélez M, Pisano ED, Jong RA, Evans WP, Morton MJ, et al. Combined screening with ultrasound and mammography vs mammography alone in women at elevated risk of breast cancer. *JAMA* 2008;**299**:2151–63.

[4] Jackson VP, Hendrick RE, Feig SA, Kopans DB. Imaging of the radiographically dense breast. *Radiology* 1993;**188**:297–301.

[5] Morrow M, Waters J, Morris E. MRI for breast cancer screening, diagnosis, and treatment. *Lancet* 2011;**378**:1804–11.

[6] Li Q, Luckner C, Hertel M, Radicke M, Maier A, et al. Combining ultrasound and x-ray imaging for mammography. In: Handels H, et al., editors. *Bildverarbeitung für die Medizin 2019*. Wiesbaden: Springer Fachmedien Wiesbaden; 2019. p. 245–50.

[7] Manohar S, Dantuma M. Current and future trends in photoacoustic breast imaging. *Photoacoustics* 2019;**16**:100134.

[8] Mehrmohammadi M, Yoon SJ, Yeager D, Emelianov SY. Photoacoustic imaging for cancer detection and staging. *Curr Mol Imaging* 2013;**2**:89–105.

[9] Quiros-Gonzalez I. Optoacoustics delineates murine breast cancer models displaying angiogenesis and vascular mimicry. *Br. J. Cancer* 2018;**118**:1098–106.

[10] Ron A, Déan-Bén XL, Gottschalk S, Razansky D. Volumetric optoacoustic imaging unveils high-resolution patterns of acute and cyclic hypoxia in a murine model of breast cancer. *Cancer Res.* 2019;**79**:4767–75.

[11] Brown E, Brunker J, Bohndiek SE. Photoacoustic imaging as a tool to probe the tumour microenvironment. *Dis Model Mech* 2019;**12**.

[12] Diot G. Multispectral optoacoustic tomography (msot) of human breast cancer. *Clin Cancer Res* 2017;**23**:6912–22.

[13] Sharma A, Srishti S, Periyasamy V, Pramanik M. Photoacoustic imaging depth comparison at 532-, 800-, and 1064-nm wavelengths: Monte Carlo simulation and experimental validation. *J Biomed Opt* 2019;**24**:1–10.

[14] Merčep E, Burton NC, Claussen J, Razansky D. Whole-body live mouse imaging by hybrid reflection-mode ultrasound and optoacoustic tomography. *Opt. Lett.* 2015;**40**:4643–6.

[15] Kim J, Park S, Jung Y, Chang S, Park J, Zhang Y, Lovell JF, Kim C. Programmable real-time clinical photoacoustic and ultrasound imaging system. *Sci Rep* 2016;**6**:35137.

[16] Oeri M, Bost W, Sénégond N, Tretbar S, Fournelle M. Hybrid photoacoustic/ultrasound tomograph for real-time finger imaging . *Ultrasound Med Biol* 2017;**43**(10):2200–12.

[17] Pérez-Liva M, Herraiz JL, Udías JM, Miller E, Cox BT, Treeby BE. Time domain reconstruction of sound speed and attenuation in ultrasound computed tomography using full wave inversion. *J. Acoust. Soc. Am.* 2017;**141**:1595–604.

[18] Taruttis A, van Dam GM, Ntziachristos V. Mesoscopic and macroscopic optoacoustic imaging of cancer. *Cancer Res.* 2015;**75**:1548–59.

[19] Déan-Bén XL, Ford SJ, Razansky D. High-frame rate four dimensional optoacoustic tomography enables visualization of cardiovascular dynamics and mouse heart perfusion. *Sci Rep* 2015;**5**:10133 EP -.

[20] Okawai H, Kobayashi K, Nitta S. An approach to acoustic properties of biological tissues using acoustic micrographs of attenuation constant and sound speed. *J Ultrasound Med* 2001;**20**:891–907.

[21] Merčep E, Herraiz JL, Dean-Ben XL, Razansky D. Transmission–reflection optoacoustic ultrasound (TROPUS) computed tomography of small animals. *Light: Sci Appl* 2019;**8**:18.

[22] Déan-Ben XL, Ntziachristos V, Razansky D. Effects of small variations of speed of sound in optoacoustic tomographic imaging. *Med Phys* 2014;**41**:073301.

[23] Razansky D, Ntziachristos V. Hybrid photoacoustic fluorescence molecular tomography using finite-element-based inversion. *Med Phys* 2007;**34**:42934301.

[24] Frangi AF, Niessen WJ, Vincken KL, Viergever MA. Multiscale vessel enhancement filtering. In: Wells WM, Colchester A, Delp S, editors. *Medical Image Computing and Computer-Assisted Intervention—MICCAI'98*. Berlin, Heidelberg: Springer Berlin Heidelberg; 1998. p. 130–7.

[25] Jespersen SK, Wilhjelm JE, Sillesen H. Multi-angle compound imaging. *Ultrasond Imag* 1998;**20**:81–102.

[26] Trots I, Nowicki A, Lewandowski M, Tasinkevych Y. *Synthetic Aperture Method in Ultrasound Imaging, Ultrasound Imaging*. IntechOpen; 2011.

[27] Li CP, Huang LJ, Duric N, Zhang HJ, Rowe C. An improved automatic time-of-flight picker for medical ultrasound tomography. *Ultrasonics* 2009;**49**:61–72.

[28] Kalkan E. An automatic P-Phase arrival-time picker. *Bull. Seismol Soc. Am.* 2016;**106**:971–86.

[29] Li CP, Duric N, Huang LJ. Comparison of ultrasound attenuation tomography methods for breast imaging. In: Proceedings Volume 6920, Medical Imaging 2008: Ultrasonic Imaging and Signal Processing. San Diego: SPIE; 2008.

[30] Perez-Liva M, Udías JM, Camacho J, Merčep E, Deán-Ben XL, Razansky D, Herraiz JL. Speed of sound ultrasound transmission tomography image reconstruction based on bézier curves. *Ultrasonics* 2020;**103**:106097.

[31] Herzog E, Taruttis A, Beziere N, Lutich AA, Razansky D, Ntziachristos V. Optical imaging of cancer heterogeneity with multispectral optoacoustic tomography. *Radiology* 2012;**263**:461–8.

[32] Merčep E, Jeng G, Morscher S, Li P, Razansky D. Hybrid optoacoustic tomography and pulse-echo ultrasonography using concave arrays. *IEEE Trans Ultrason Ferroelectr Freq Control* 2015;**62**:1651–61.

[33] Dean-Ben XL, Buehler A, Ntziachristos V, Razansky D. Accurate model-based reconstruction algorithm for three-dimensional optoacoustic tomography. *IEEE Trans Med Imag* 2012;**31**(10):1922–8.

[34] Li C, Duric N, Littrup P, Huang L. In vivo breast sound-speed imaging with ultrasound tomography. *Ultrasound Med Biol* 2009;**35**:1615–28.

[35] Tomaszewski MR, Gehrung M, Joseph J, Quiros-Gonzalez I, Disselhorst JA, Bohndiek SE. Oxygen-enhanced and dynamic contrast-enhanced optoacoustic tomography provide surrogate biomarkers of tumor vascular function, hypoxia, and necrosis. *Cancer Res.* 2018;**78**:5980–91.

[36] Wilson KE, Valluru KS, Willmann JK. Nanoparticles for Photoacoustic Imaging of Cancer. Cham: Springer International Publishing; 2017. p. 315–35.

[37] Madsen HHT, Rasmussen F. Contrast-enhanced ultrasound in oncology. *Cancer Imag* 2011;**11**:S167–73.

[38] Jang H-J, Yu H, Kim TK. Contrast-enhanced ultrasound in the detection and characterization of liver tumors. *Cancer Imag* 2009;**9**:96–103.

[39] Alamo L, Fischer U. Contrast-enhanced color doppler ultrasound characteristics in hypervascular breast tumors: comparison with MRI. *Eur Radiol* 2001;**11**:970–7.

[40] Déan-Bén XL, Merčep E, Razansky D. Hybrid-array-based optoacoustic and ultrasound (OPUS) imaging of biological tissues. *Appl Phys Lett* 2017;**110**:203703.

[41] Sak M, Duric N, Littrup P, Bey-Knight L, Ali H, Vallieres P, Sherman ME, Gierach GL. Using speed of sound imaging to characterize breast density. *Ultrasound Med Biol* 2017;**43**:91–103.

[42] Schoustra SM, Piras D, Huijink R, op't Root TJPM, Alink L, Kobold WMF, Steenbergen W, Manohar S. Twente photoacoustic mammoscope 2: system overview and threedimensional vascular network images in healthy breasts. *J Biomed Opt* 2019;**24**:1–12.